

Antiferromagnetism-induced second-order nonlinear optical responses of centrosymmetric bilayer CrI_3

Vijay Kumar Gudelli¹ and Guang-Yu Guo^{2,1}

¹ Physics Division, National Center for Theoretical Sciences, Hsinchu 30013, Taiwan

² Department of Physics and Center for Theoretical Physics, National Taiwan University, Taipei 10617, Taiwan

E-mail: gyguo@phys.ntu.edu.tw

Abstract. Antiferromagnetism (AF) in AB' -stacked centrosymmetric bilayer (BL) CrI_3 breaks both spatial inversion (P) and time-reversal (T) symmetries but maintains the combined PT symmetry, thus inducing novel second-order nonlinear optical (NLO) responses such as second-harmonic generation (SHG), linear electric-optic effect (LEO) and bulk photovoltaic effect (BPVE). In this work, we calculate AF-induced NLO responses of the BL CrI_3 based on the density functional theory with the generalized gradient approximation (GGA) plus onsite Coulomb correlation (U), i.e., the GGA+U method. Interestingly, we find that the magnetic SHG, LEO and photocurrent in the AF BL CrI_3 are huge, being comparable or even larger than that of the well-known nonmagnetic noncentrosymmetric semiconductors. For example, the calculated SHG coefficients are in the same order of magnitude as that of MoS_2 monolayer (ML), the most promising 2D material for NLO devices. The calculated LEO coefficients are almost three times larger than that of MoS_2 ML. The calculated NLO photocurrent in the CrI_3 BL is among the largest values predicted so far for the BPVE materials. On the other hand, unlike nonmagnetic semiconductors, the NLO responses in the AF BL CrI_3 are nonreciprocal and also switchable by rotating magnetization direction. Therefore, our interesting findings indicate that the AF BL CrI_3 will not only provide a valuable platform for exploring new physics of low-dimensional magnetism but also have promising applications in magnetic NLO and LEO devices such as frequency conversion, electro-optical switches, and light signal modulators as well as high energy conversion efficiency photovoltaic solar cells.

1. Introduction

Recently, two groups discovered long-range magnetic orders in atomically thin films of semiconductors CrGeTe_3 [1] and CrI_3 [2]. This exciting discovery has opened up new research directions for two-dimensional (2D) materials. In particular, magnetism at 2D limit is highly desirable for both the fundamental physics and also for the technological applications ranging from magnetic memories to sensing, to spintronics to novel functionalities based on 2D materials. Consequently, magnetic 2D materials are currently subject to intensive investigations. Among the magnetic 2D materials, bilayer (BL) CrI_3 seems to be unique and attracts particularly strong attention [3–9]. Unlike other atomically thin films of CrGeTe_3 and CrI_3 which exhibit a ferromagnetic long-range order, [1,2], BL CrI_3 shows an interlayer antiferromagnetic (AF) order [2]. This AF order in BL CrI_3 leads to a number of emerging phenomena, such as giant tunnelling magnetoresistance in spin-filter tunnel junctions [8,9] and the electrical control of 2D magnetism [4–6]. First-principles density functional theory studies [10–13] indicated that the interlayer magnetic coupling in BL CrI_3 is highly stacking dependent [10–13] and that the unusual AF coupling originates from the monoclinic AB' stacking [see Fig. 1(c)] in BL CrI_3 instead of the usual trigonal AB stacking [see Fig. 1(b)] in other CrI_3 multilayers.

Very recently, giant nonreciprocal second-harmonic generation (SHG) was observed in the AF BL CrI_3 [14]. SHG converts two incident photons of the same frequency (ω) into a new photon with a doubled frequency (2ω), and is a second-order nonlinear optical phenomenon [15,16]. SHG plays an important role in the modern optics and electro-optical devices such as lasers, electro-optical modulators and switches, frequency conversions [15,16]. Second-order NLO phenomena occur in nonmagnetic materials with the broken spatial inversion (P) symmetry. [15,16] The AB' stacked BL CrI_3 has the centrosymmetric C_{2h} symmetry group [see Fig. 1(c)], and nonmagnetic AB' stacked BL CrI_3 would not exhibit second-order NLO responses. Intriguingly, the antiferromagnetism in the AB' stacked BL CrI_3 breaks both time-reversal (T) and spatial inversion symmetries [14] [see Fig. 1(d)] but maintains the combined PT symmetry [17]. This results in a number of emergent magnetic NLO responses such as magnetic SHG reported in Ref. [14] and opens up possibilities for the application of magnetic 2D materials in magnetic controllable NLO and nonreciprocal optical devices.

In this work, we calculate three AF-induced NLO responses of the BL CrI_3 , namely, SHG, linear electric-optic effect (LEO) and nonlinear injection photocurrent. Our calculations are based on the density functional theory with the generalized gradient

approximation (GGA) plus onsite Coulomb correlation (U), i.e., the GGA+U method. Interestingly, we find that the present calculated magnetic SHG, LEO and photocurrent in the AF BL CrI_3 are huge in comparison with the well-known nonmagnetic noncentrosymmetric semiconductors with the same properties. In particular, the calculated SHG coefficients of the AF BL CrI_3 are in the same order of magnitude as that of MoS_2 monolayer (ML), which is the best candidate of the NLO material among the 2D materials. Further, the calculated LEO coefficients derived from SHG coefficients, are almost three times higher than the reported LEO coefficients of MoS_2 ML. We observe that the NLO photocurrent in BL CrI_3 is robust and it is one of the highest values predicted so far for the BPVE materials. Interestingly, we also find that the NLO responses in the AF BL CrI_3 are nonreciprocal and also reversible by rotating magnetization direction, which is very different from the nonmagnetic NLO semiconductors. This work thus demonstrates that because of its novel AF-induced NLO properties, AF BL CrI_3 will find promising applications in magnetic based NLO devices such as electro-optical switches, frequency conversion and light signal modulators as well as high energy conversion efficiency photovoltaic solar cells.

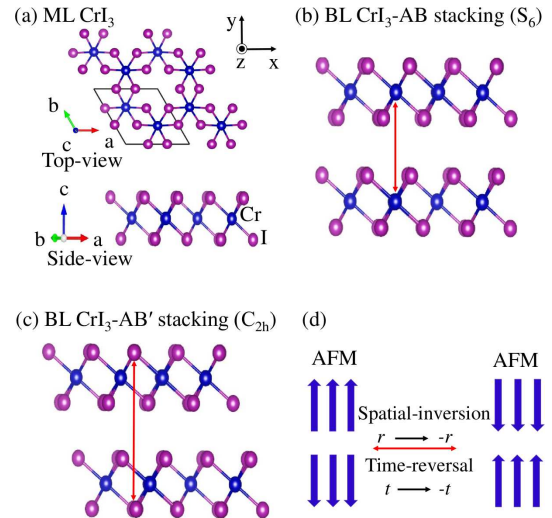


Figure 1. (a) Top and side view of ML CrI_3 . The black solid line denotes the primitive cell. (b) The AB stacked BL CrI_3 with rhombohedral symmetry of S_6 point group. (c) The AB' stacked BL CrI_3 with monoclinic symmetry of C_{2h} point group. This structure can be obtained by a lateral shift of bottom layer of the AB stacked BL CrI_3 in (b). (d) Schematic representation of the interlayer AF configuration in the AB' stacked BL CrI_3 and the effects of the P and T symmetry operations.

2. Theory and computational methods

Bulk CrI_3 forms a layered structure with the monolayers (MLs) separated by the van der Waals gap. Each CrI_3 ML consists of edge-sharing CrI_6 octahedra forming a planar network with Cr atoms in a honeycomb lattice [Figs 1(a)]. These MLs are then stacked in an ABC sequence, resulting in a rhombohedral crystal with $R\bar{3}$ symmetry. This structure can also be regarded as an ABC-stacked hexagonal crystal with experimental lattice constants $a = 6.867 \text{ \AA}$ and $c = 19.807 \text{ \AA}$ [18]. For the CrI_3 BL structure, the two CrI_3 MLs can be stacked in two ways, namely, the AB stacking with S_6 symmetry and the AB' with C_{2h} symmetry with the y -axis being the in-plane C_2 axis, as shown in Figs. 1(b) and 1(c), respectively. The monoclinic AB' stacking is constructed using the AB stacked BL by a lateral shift of the bottom CrI_3 ML. We have studied the magnetic and magneto-optical properties of the AB stacked CrI_3 BL before [19]. Zhang *et al.* have calculated the NLO photocurrents in the AB stacked CrI_3 BL [17]. In this paper, we consider only the monoclinic AB' stacked CrI_3 BL in the layered antiferromagnetic structure [(see Fig. 1(d)], since it is the experimentally observed crystalline structure for the AF BL CrI_3 [14]. Furthermore, we have calculated the total energies of the intralayer FM as well as intralayer AF-Neel, AF-zigzag and AF-stripe magnetic configurations [19], and we found that all the intralayer AF structures have a total energy much higher than that of the FM structure (at least 280 meV/cell higher), indicating that the intralayer AF structures are unlikely to occur. The slab-superlattice approach is used to simulate the BL structure with the separation of the neighboring BLs being 15 \AA .

The electronic band structure, magnetic and optical properties of BL CrI_3 are calculated based on first-principles density functional theory with the GGA [20]. To better describe the Coulomb correlation among the Cr 3d electrons, we adopt the GGA+ U scheme [21]. Following the recent studies [19, 22], we use $U = 1.0 \text{ eV}$ in the present calculations. The calculations are performed using the accurate projector-augmented wave (PAW) method [23, 24], as implemented in the Vienna *ab-initio* simulation package (VASP) [25, 26]. The fully relativistic PAW potentials are adopted in order to include the SOC effect. A large plane-wave energy cutoff of 400 eV is used in all the calculations. For the Brillouin zone integration, a k -point mesh of $20 \times 20 \times 1$ is used. All the calculations are performed with an energy convergence within 10^{-6} eV between the successive iterations.

The optical properties are calculated based on the linear response formalism with the independent-

particle approximation (IPA) in which the interaction between the electromagnetic field and the electrons in the solid is treated as a perturbation. Aversa and Sipe have developed a compact length-gauge formulation for calculating the nonlinear optical properties such as the SHG, shift and injection currents of general solids including magnetic materials [27]. Here we use the slightly re-arranged expressions from Ref. [27]. In particular, the second-harmonic polarization density is given by $P_a^{(2)}(\omega) = \chi_{abc}^{(2)}(-2\omega; \omega, \omega) \mathcal{E}_b(\omega) \mathcal{E}_c(\omega)$ where $\mathcal{E}_b(\omega)$ denotes the cartesian b -component of the optical electric field and $\chi_{abc}^{(2)}(-2\omega, \omega, \omega)$ is the SHG susceptibility. The $\chi_{abc}^{(2)}(-2\omega; \omega, \omega)$ can be written as

$$\chi_{abc}^{(2)}(-2\omega; \omega, \omega) = \chi_{abc,i}^{(2)}(-2\omega; \omega, \omega) + \chi_{abc,e}^{(2)}(-2\omega; \omega, \omega), \quad (1)$$

where

$$\chi_{abc,e}^{(2)} = \frac{e^3}{\epsilon_0 \hbar^2 V_c} \sum_{n,m,l} \sum_{\mathbf{k}} \frac{r_{nm}^a}{\omega_{mn} - 2\omega} \left(\frac{r_{ml}^b r_{ln}^a f_{nl}}{\omega_{ln} - \omega} - \frac{r_{ml}^c r_{ln}^b f_{lm}}{\omega_{ml} - \omega} \right) \quad (2)$$

is the contribution of the purely interband processes and

$$\chi_{abc,i}^{(2)} = \frac{ie^3}{\epsilon_0 \hbar^2 V_c} \sum_{n,m} \sum_{\mathbf{k}} \left(\frac{f_{nm} r_{nm}^a}{\omega_{mn} - 2\omega} \left(\frac{r_{mn;b}^c}{\omega_{mn} - \omega} - \frac{r_{mn}^c \Delta_{mn}^b}{\omega_{mn} - \omega} \right) - \frac{f_{nm} r_{mn}^c}{2(\omega_{mn} - \omega)} \left(\frac{r_{nm;a}^b}{\omega_{mn} + \omega} - \frac{r_{nm}^b \Delta_{mn}^a}{(\omega_{ml} - \omega)^2} \right) \right) \quad (3)$$

is the contribution of the mixed interband and intraband processes. Here r_{nm}^a and $r_{nm;b}^a$ are the a -component of the interband position matrix element and its generalized momentum derivative, respectively. $\omega_{mn} = (\epsilon_{m\mathbf{k}} - \epsilon_{n\mathbf{k}})/\hbar$ where $\epsilon_{m\mathbf{k}}$ is the m th band energy at the \mathbf{k} point. $f_{mn} = f(\epsilon_{m\mathbf{k}}) - f(\epsilon_{n\mathbf{k}})$ where $f(\epsilon_{m\mathbf{k}})$ is the Fermi function. ϵ_0 and V_c are the vacuum permittivity and unit cell volume, respectively.

Linear electric-optic (LEO) effect refers to the linear refractive index variation (Δn) with the applied electric field strength, $\Delta n = n^3 r \mathcal{E}/2$, where n is the refraction index and r is the LEO coefficient. The LEO effect thus allows to exploit an electrical signal to control the amplitude, phase or direction of a light beam in the NLO material, leading to applications in high-speed optical modulation and sensing devices [28]. In the zero frequency limit, the LEO coefficient is given by

$$r_{abc}(0) = -\frac{2}{\epsilon_a(0)\epsilon_b(0)} \lim_{\omega \rightarrow 0} \chi_{abc}^{(2)}(-2\omega, \omega, \omega). \quad (4)$$

The LEO coefficient obtained from the SHG spectrum is referred as the electronic contribution. There are also ionic and piezoelectric contributions to the LEO effect, [29] which are out of scope of the present paper.

Another interesting second-order NLO response is the generation of DC photocurrents [30, 31]. These

photocurrents are the main contributions to the bulk photovoltaic effect (BPVE). In the IPA, these photocurrents are given by [30, 31]

$$J_a(0) = \sigma^{abc}(0; \omega, -\omega) \mathcal{E}_b(\omega) \mathcal{E}_c(-\omega). \quad (5)$$

In a nonmagnetic solid, the real part of the photoconductivity σ^{abc} gives rise to the photocurrent due to purely linearly polarized light, known as linear shift current, while the imaginary part produces photocurrent due to purely circularly polarized light, known as circular injection current [30, 31]. However, in a PT -symmetric magnetic material such as the AF CrI_3 BL, both the linear shift current and circular injection currents would be zero [32]. Instead, there are so-called circular shift current and linear injection current. The inject photocurrent conductivity σ^{abc} for a magnetic system is given by [27, 32] $\sigma^{abc} = \tau \eta_{abc}$ where τ is the photoexcited carrier relaxation time and

$$\eta_{abc} = \frac{-2\pi e^3}{\hbar^2 V_c} \sum_{\mathbf{k}} \sum_{n,m} f_{nm} \Delta_{mn}^a r_{mn}^b r_{nm}^c \delta(\omega_{mn} - \omega). \quad (6)$$

The shift photocurrent conductivity for a magnetic solid is given by [27, 32]

$$\sigma_{abc} = \frac{-i\pi e^3}{\hbar^2 V_c} \sum_{\mathbf{k}} \sum_{n,m} f_{nm} (r_{mn}^b r_{nm;a}^c - r_{nm}^c r_{mn;a}^b) \delta(\omega_{mn} - \omega). \quad (7)$$

Since a large number of k -points are needed to get accurate NLO responses [33–36], we use the efficient Wannier interpolation method based on maximally localized Wannier functions (MLWFs) [37–39]. Total 112 MLWFs per unit cell of Cr d and I p orbitals are constructed by fitting to the GGA+U+SOC band structure. The band structure obtained by the Wannier interpolation is nearly identical to that from the GGA+U+SOC calculation. The SHG susceptibility and shift current conductivity are then evaluated by taking a very dense k -point mesh of $200 \times 200 \times 1$. The unit-cell volume V_c in Eqs. (2), (3) and (6) is not well-defined for a two-dimensional (2D) system. Therefore, following the previous studies, [19, 22], we used the effective unit-cell volume of the BL rather than the volume of the supercell which is arbitrary.

3. Results and discussion

We first study the magnetic properties of the AF CrI_3 BL. The calculated spin magnetic moment on each Cr atom is $\pm 3.21 \mu_B$, being in good agreement with the experimental value of $\sim 3.0 \mu_B$ [18]. The calculated magnetic moment of Cr is also consistent with three unpaired electrons in its t_{2g} configuration in this structure. We also find significant proximity-induced magnetic moment of $\pm 0.09 \mu_B$ on the I ion.

Nevertheless, the sum of all the magnetic moments on the I and Cr sites in the unit cell is zero.

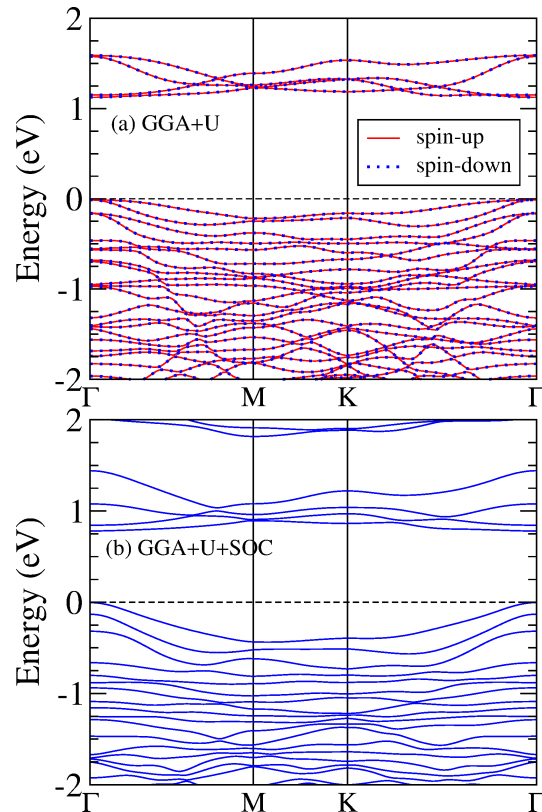


Figure 2. (a) Spin-polarized scalar-relativistic and (b) fully relativistic band structures of BL CrI_3 . Horizontal dashed-lines denote the top of valance band.

3.1. Electronic structure

A better understanding of the optical properties can be achieved through a detailed analysis of the band structure. Therefore, we display scalar-relativistic (Fig. 2(a)) and fully relativistic (Fig. 2(b)) band structures of BL CrI_3 in Fig. 2. Overall, the scalar-relativistic and fully relativistic band structures look rather similar. In particular, all the bands remain doubly degenerate, i.e., Kramers degeneracy is maintained. In the scalar-relativistic case, this is consistent with the antiferromagnetism in a centrosymmetric crystal. In the fully-relativistic case, this is somewhat surprising because the AF configuration here breaks both T symmetry and P symmetry [14]. Nevertheless, further analysis indicates that AF BL CrI_3 has the PT symmetry [17], which protects the Kramers degeneracy. However, the energy positions and shapes of some energy bands do change significantly when the SOC is included. Although Fig. 2 shows that both band structures are a semiconductor with the direct band gap located at the Γ point, the

fully relativistic band structure has a band gap of 0.78 eV, being smaller than that of the scalar-relativistic one (1.04 eV). The most important effect of the SOC is that the NLO responses of AF BL CrI₃ studied in this paper occur only when the SOC is taken into account. This is because the electrons in AF BL CrI₃ would only feel the broken P -symmetry caused by the AF configuration when the SOC is included. Therefore, all the optical properties of AF BL CrI₃ presented below are calculated from the fully relativistic band structure.

We present the total as well as site- and orbital-projected densities of states (DOS) for BL CrI₃ in Fig. 3. It is clear from Fig. 3 that the valance and conduction bands in the energy ranges between -3.0 and 0.0 eV as well as between 1.0 eV and 3.0 eV, respectively, are dominated by the Cr d orbitals with a significant contribution from the I p orbitals, suggesting the strong hybridization between Cr d and I p orbitals in the CrI₃ structure. Specifically, the upper valance band region between -1.75 eV and 0.0 eV are made up of Cr t_{2g} (i.e., d_{xy}, x^2-y^2 and d_{z^2}) orbitals. The lower conduction bands ranging from 1.0 eV to 1.6 eV stem mainly from the Cr e_g (i.e., d_{xz}, yz) orbitals (see Fig. 3(b)). This indicates that the band gap in the CrI₃ structure is caused by the crystal-field splitting of the Cr t_{2g} and e_g bands. The conduction bands ranging from 1.75 eV to 3.0 eV are made up mainly of the Cr d_{xy}, x^2-y^2 and d_{z^2} orbitals.

It is well-known that the band gap calculated based on the GGA functional is usually too small compared with the experimental one, mainly because the many-body effects especially quasiparticle self-energy correction are not fully taken into account in the GGA. For example, the GGA band gap of bulk CrI₃ is 0.62 eV [19] being about 50 % smaller than the experimental value of 1.2 eV [40]. Nonetheless, semilocal hybrid Heyd-Scuseria-Ernzerhof (HSE) functional [41, 42] is known to produce improved band gaps for semiconductors. We have performed the HSE calculations for bulk and multilayer CrI₃ using the HSE06 functional [19]. Indeed, we obtained the HSE band gap of 1.22 eV for bulk CrI₃, being in excellent agreement with the experimental value. Therefore, in the present calculations of the optical and NLO properties, we use the HSE band gap of 1.33 eV for BL CrI₃ and then adopt the scissors correction (SC) scheme.

3.2. Dielectric function

To help understand the calculated SHG and photocurrent of BL CrI₃ and also to estimate the linear electro-optical effect, we also calculate the linear optical properties. The calculated real ($\epsilon'(\omega)$) (dispersive) and imaginary ($\epsilon''(\omega)$) (absorptive) part of the optical dielectric function of the BL CrI₃

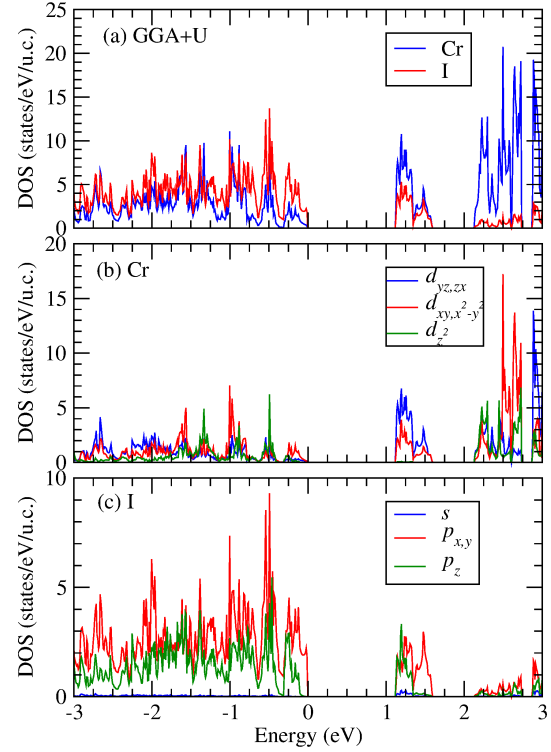


Figure 3. Site- and orbital-projected densities of states (DOS) of BL CrI₃ from the scalar-relativistic calculation.

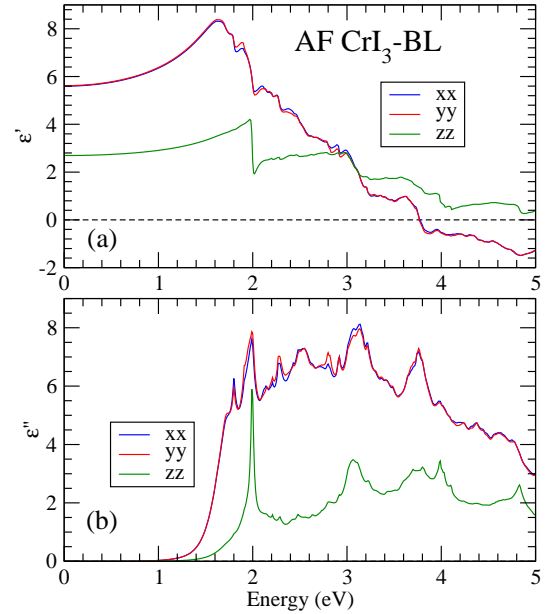


Figure 4. (a) Real and (b) imaginary parts of the dielectric function of BL CrI₃.

are presented in Fig. 4. Notably, the dielectric function of out-of-plane electric polarization ϵ_{zz} ($\mathcal{E}||c$) differs significantly from that of two in-plane electric polarizations ϵ_{xx} and ϵ_{yy} (note that $x||a$), although the

latter two are nearly identical (see Fig. 4). This strong optical anisotropy is expected from the 2D nature of the BL CrI₃ structure. Specifically, in the case of the real part of the dielectric constant, the two in-plane polarization ones (ϵ'_{xx} and ϵ'_{yy}) are nearly twice as large as that of the out-of-plane electric polarization one (ϵ'_{zz}) in the photon energy from 0.0 to 2.0 eV. As the photon energy further increases, this difference steadily reduces and at ~ 3.0 eV or above, ϵ'_{zz} becomes larger than ϵ'_{xx} and ϵ'_{yy} [see Fig. 4(a)]. In the case of the imaginary part of the dielectric constant, ϵ''_{xx} and ϵ''_{yy} start to increase sharply at ~ 1.4 eV until 2.0 eV, while ϵ''_{zz} starts to increase rapidly only at ~ 1.8 eV. In the photon energy range from 2.0 eV to 5.0 eV, ϵ''_{xx} and ϵ''_{yy} are about two-times larger than ϵ''_{zz} .

This strong anisotropy in the linear optical property of bulk and multilayers CrI₃ was noticed before in, e.g., the previous study of Ref. [19]. This behavior of the linear optical property can be understood in terms of the calculated orbital-decomposed DOS presented in the proceeding section. In the energy range of -3 to -0.3 eV in the valence band region, the energy bands are dominated by the Cr *d* orbitals [see Fig. 3(b)], with a major contribution from the d_{xy, x^2-y^2} orbitals. It was shown [19] that d_{xy, x^2-y^2} (d_{z^2}) states can be excited by only $\mathcal{E} \perp c$ ($\mathcal{E} \parallel c$) polarized light while Cr $d_{xz, yz}$ orbitals can be excited by light of both polarization. This suggests that ϵ'_{xx} usually is greater than ϵ'_{zz} in the low energy region (see Fig. 4).

3.3. Second-harmonic generation

Symmetry considerations allow us to identify nonzero elements of the third-rank SHG susceptibility tensor. The AB' stacked BL CrI₃ has the centrosymmetric C_{2h} ($2/m$) space group and consequently should not have any second-order NLO responses. As mentioned before, however, the AF structure breaks the spatial inversion and time-reversal symmetries, resulting in a magnetic space group of C_2 ($2'$). The C_2 magnetic space group has ten nonvanishing elements in the SHG susceptibility tensor [43]. By considering the elements of the SHG susceptibility with only the *xy*-plane polarizations (i.e., considering only the normal incidence), we are left with only three independent non-zero elements, namely, $\chi_{xxx}^{(2)}$, $\chi_{xyy}^{(2)}$, $\chi_{yxy}^{(2)}$. The calculated real, imaginary and absolute values of these three non-vanishing elements of BL CrI₃ are presented in Fig. 5.

As expected, Fig. 5(b) shows that the imaginary (absorptive) part of the $\chi^{(2)}$ spectra of all the three elements is zero for photon energy ($\hbar\omega$) below 0.67 eV (mid-band gap). As $\hbar\omega$ further increases, the imaginary part increases sharply in magnitude and reaches its maximum just above 0.8 eV. After that, the

magnitudes of the imaginary part of all the elements decreases oscillatorily all the way up to 5.0 eV. The magnitude of the real part and absolute value of the $\chi^{(2)}$ spectra are not zero at $\hbar\omega = 0$ and increases gradually with $\hbar\omega$ up to ~ 0.67 eV. When $\hbar\omega$ further increases, they increase dramatically and reaches the maximum at ~ 0.8 eV (see Fig. 5(a)). Among the three elements, we find that the magnitude of the imaginary part and absolute value of $\chi_{xxx}^{(2)}$ is more or less larger than the other two elements in the energy range from 0.0 to 3.0 eV (see Fig. 5(c)). In particular, the maximum absolute value of the $\chi_{xxx}^{(2)}$ is as large as ~ 350 pm/V at $\hbar\omega = 0.85$ eV. We also notice that $\chi_{xyy}^{(2)}$ has a sharp narrow peak with its absolute value of ~ 350 pm/V at 1.7 eV.

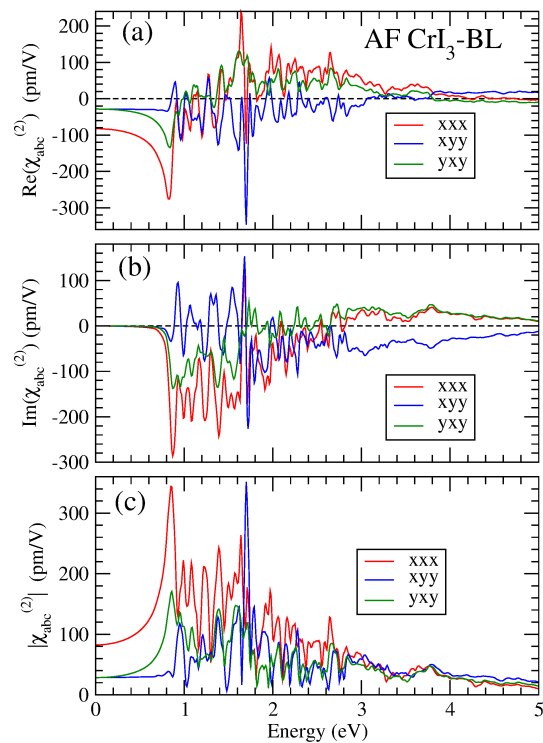


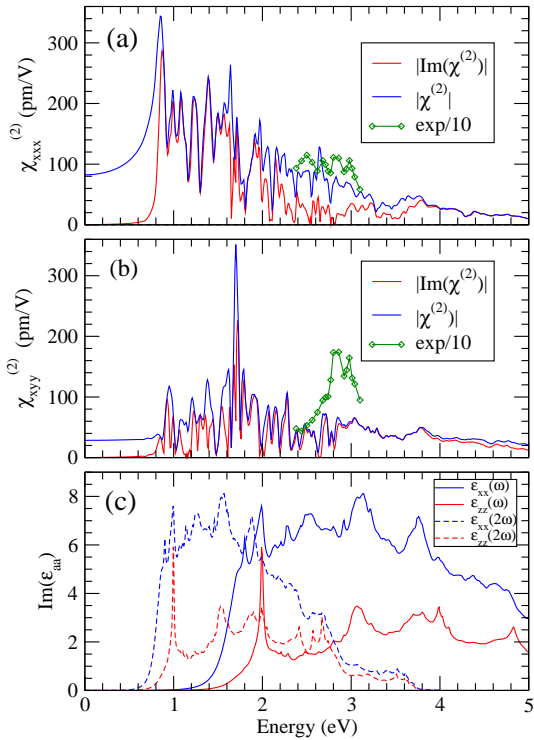
Figure 5. (a) Real, (b) imaginary and (c) absolute value of the SHG spectra of BL CrI₃.

To analyze the origins of the prominent features in the calculated SHG spectra, we display the modulus of the imaginary part and absolute value of the second-order susceptibilities $|\chi^{(2)}(-2\omega, \omega, \omega)|$ together with the imaginary part of the dielectric functions $\epsilon''(\omega)$ and $\epsilon''(2\omega)$ in Fig. 6. Figure 6(a) and (b) shows that the peaks in the $|Im[\chi^{(2)}(-2\omega, \omega, \omega)]|$ in the energy range from the mid-band gap (~ 0.67 eV) to the absorption edge (~ 1.33 eV) can be correlated with the features in the $\epsilon''(2\omega)$ spectra (see Fig. 6(c)), indicating that they are due to double-photon (2ω) resonances. The peaks above the absorption edge, on the other hand,

Table 1. Calculated dielectric constant ($\varepsilon_{yy} \approx \varepsilon_{xx}$), second-order optical susceptibility ($\chi_{abc}^{(2)}$), and linear electro-optical coefficient (r_{abc}) of BL CrI₃.

$\hbar\omega$ (eV)	ε_{xx}	ε_{zz}	$\chi_{xxx}^{(2)}$ (pm/V)	$\chi_{xyx}^{(2)}$ (pm/V)	$\chi_{yyx}^{(2)}$ (pm/V)	r_{xxx} (pm/V)	r_{xyx} (pm/V)	r_{yyx} (pm/V)
0.0	5.60	2.69	-82.5	-28.5	-28.5	5.26	1.82	1.82
0.7	5.93	2.79	159	31.9	67.6	10.1	2.03	4.31

can be related to the features in either the $\varepsilon''(2\omega)$ or $\varepsilon''(\omega)$ or even both, suggesting that they can be caused by both double-photon and single-photon resonance. Because of the contributions from both one- and two-photon resonances, the spectra oscillate rapidly in this region and diminish gradually at higher photon energies. Both the spectrum of $\chi_{xxx}^{(2)}$ and $\chi_{xyy}^{(2)}$ elements have almost the same oscillatory behavior.

**Figure 6.** Modulus and absolute value of the imaginary part of the second-order susceptibility of (a) $\chi_{xxx}^{(2)}$ and (b) $\chi_{xyy}^{(2)}$ of BL CrI₃. (c) Imaginary part of the dielectric function ε'' of BL CrI₃. Solid line with green diamonds in (a) and (b) represents the experimental SHG spectrum from Ref. [14]. The experimental SHG spectra are scaled by a factor of 1/10.

The SHG coefficients of some bulk AF materials such as the classic PT -symmetric Cr₂O₃ have been measured before. We notice that compared with these bulk materials, the magnetic SHG coefficients of the BL CrI₃ are gigantic, being two-orders of magnitude larger than that of Cr₂O₃ (~ 2 pm/V) [14].

Furthermore, we notice that the surface/interface-induced SHG in the ferromagnetic thin-films is even smaller, being in the order of 0.4×10^{-7} pm/V [44, 45]. The magnetic SHG found in the BL CrI₃ is nonreciprocal and also the sign of the SHG is controllable by switching the magnetization direction [14]. Therefore, the large SHG found in the BL CrI₃ suggests that the BL CrI₃ will have valuable applications in magneto-optical NLO devices.

Let us now compare the SHG of the present material with that of other 2D materials. First we notice that the modulus of $\chi_{xxx}^{(2)}$ at zero frequency in BL CrI₃ is two times larger than $\chi_{yyy}^{(2)}$ of the BN sheet [34, 35], although it is nearly three times smaller than $\chi_{yyy}^{(2)}$ of the SiC sheet [36]. Wang and Guo [33] recently performed systematic *ab initio* studies of the second-order NLO responses of odd number few-layers of group 6B transition metal dichalcogenides. The spatial inversion symmetry in these odd number few-layer structures is broken and thus gives rise to large SHG coefficient and also significant LEO effect [33]. Strikingly, the magnetic SHG spectra of the AF CrI₃ BL (Figs. 5 and 6) are in the same order of magnitude as that of monolayer MoS₂ [33], which is the best candidate of the NLO material among the 2D materials [46–48]. This demonstrates that the magnetism-induced SHG in a centrosymmetric crystal can be as large as that of a crystal with the broken P symmetry. Thus the excellent nonreciprocal NLO properties of the AF BL CrI₃ will find promising applications in ultrathin light signal modulators, second-harmonic and sum-frequency generation devices and in electro-optical switches.

As mentioned above, the SHG experiments on the AF CrI₃ BL have been very recently carried out [14]. The experimental $\chi_{xxx}^{(2)}$ and $\chi_{xyy}^{(2)}$ spectra are re-plotted, respectively, in Figs. 6(a) and 6(b) for comparison. Figure 6 shows that overall, the peak positions and line shapes of the calculated SHG spectra are in good agreement with the experimental spectra. Nonetheless, the measured SHG spectra are generally one-order of magnitude larger than the calculated spectra. The discrepancy in the magnitude of the spectra between the experiment and the present theory might be due to the fact that in the present calculation a free-standing

CrI₃ BL is considered, whereas in the experiment [14] the mechanical exfoliated CrI₃ was put on the substrate of Si/SiO₂ and was also encapsulated by hBN thin flakes [14]. We notice that the sample preparation of a 2D material can have a significant effect on the optical and NLO responses of the 2D material. For example, the presence of the interface between the substrate and the material may break the inversion symmetry of the substrate and thus induces additional non-vanishing SHG spectra [49–51]. This suggests that further SHG measurements on the AF BL CrI₃ structure are needed to resolve this discrepancy. Moreover, the experimental reported $\chi^{(2)}$ values of ML MoS₂ can vary as much as three-orders of magnitude. The experiential $|\chi^{(2)}|$ at 810 nm wavelength of the mechanically exfoliated ML MoS₂ reported in Ref. [49] is as large as $\sim 10^5$ pm/V, while the ML-MoS₂ prepared by chemical vapor deposition has the $\chi^{(2)}$ value of 5×10^3 pm/V [47] and in another experiment the value of $\chi^{(2)}$ was reported to be about 320 pm/V [46].

3.4. Linear electro-optical coefficient

The LEO effect has been used extensively in the integrated optical devices for optical communications and modulating light. Thus, we also calculate the LEO coefficient of BL CrI₃ using the obtained dielectric constants and SHG susceptibility [see Eq. (4)]. The calculated LEO coefficients $r_{abc}(0)$ at photon energy of zero and 0.7 eV, along with the corresponding dielectric constants and SHG coefficients are presented in Table 1. Interestingly, there is a strong in-plane anisotropy in both the SHG and LEO coefficients (see Table 1). Furthermore, all the static r_{abc} values of BL CrI₃ are significantly larger than the corresponding elements of r_{abc} of the MLs of transition metal dichalcogenide semiconductors [33]. In particular, the modulus of r_{xxx} of BL CrI₃ (5.26 pm/V) is more than four times larger than that of r_{xxy} of ML MoS₂ (1.23 pm/V) [33]. We also notice that this value is three times larger than that of the BN sheet [34, 35]. This is somewhat surprising since the magnetism-induced second-order NLO responses are expected to be smaller than that due to the broken inversion symmetry in the crystal structure. Thus, the significant nature of the magnetism-induced SHG spectra and LEO coefficients of BL CrI₃ would enable it to find promising applications in magnetic material-based optical communications.

3.5. Shift and injection photocurrents

As discussed above in Sec. 2, in the AF BL CrI₃, because of its PT symmetry, there is no nonvanishing element of usual linear shift photocurrent tensor and circular injection photocurrent which occur

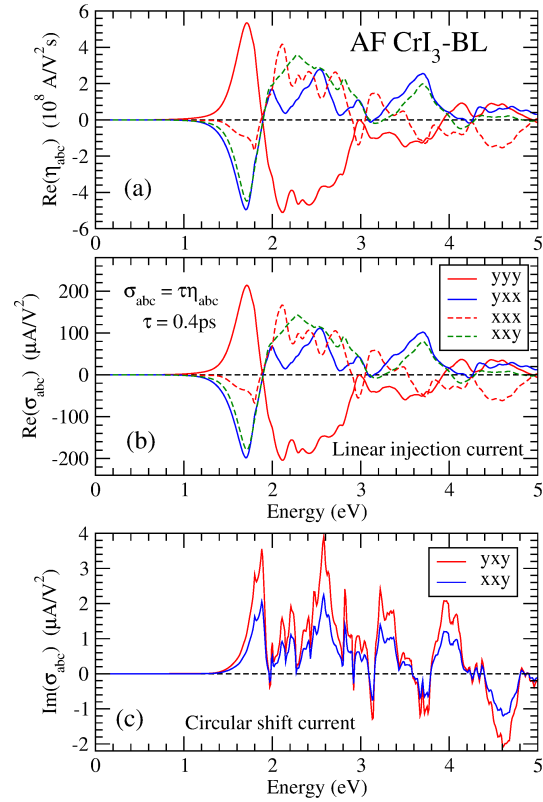


Figure 7. (a) Injection photocurrent susceptibility η_{abc} and (b) conductivity σ_{abc} of BL CrI₃. (c) Shift photocurrent conductivity of BL CrI₃.

in nonmagnetic broken P -symmetry materials [32]. However, there are nonzero elements of circular shift current and linear injection current instead. Here we consider only the in-plane polarizations of optical electric field and the in-plane photocurrents. Consequently, we have six independent nonzero elements of the linear injection current tensor [43], namely, xxx, xyy, xxy, yxx, yyy and yxy . We display four pronounced nonzero elements of the calculated injection current susceptibility η_{abc} in Figs. 7(a). Note that in the AB-stacked AF BL CrI₃, there are only two independent in-plane nonzero elements of the linear injection current tensor, [17] namely, σ_{xxx} and σ_{yyy} . Using the typical relaxation time of $\tau = 0.4$ ps [17], we obtain the injection photocurrent conductivity σ_{abc} [see Eq.(6) in Sec. 2], as shown in Fig. 7(b). There are also two independent in-plane nonzero elements of circular shift current tensor, as displayed in Fig. 7(c). In contrast, there is no nonzero element of circular shift current tensor in the AB-stacked AF BL CrI₃ [17]. These additional nonzero elements of the photoconductivity tensors in the AB'-stacked CrI₃ BL studied here will allow one to characterize the structure of the CrI₃ BL by the BPVE experiments.

Overall, the spectra of all the four σ_{abc} (η_{abc})

elements displayed in Fig. 7(b) [7(a)] have quite similar shapes and magnitudes. However, the yyy spectrum has the opposite sign to that of the rest three spectra over almost the entire energy range. They are all zero below the band gap of 1.33 eV and they increase rapidly above the absorption edge. In particular, σ_{yyy} , σ_{yxx} and σ_{xxy} reach their maximum of $\sim 210 \mu\text{A}/\text{V}^2$ at ~ 1.71 eV. As the photon energy further increases, σ_{yyy} decreases rapidly, changing sign at ~ 1.89 eV and reaches its negative maximum of $-204 \mu\text{A}/\text{V}^2$ at 2.12 eV. We notice that our yxx linear injection current spectrum is similar in both magnitude and shape to the yyy spectrum of the AB-stacked CrI₃ BL reported by Zhang *et al.* [17]. The magnitude of our yyy spectrum is similar to that of both xxx and yyy spectra in [17].

The two circular shift current spectra are almost identical in shape [see Fig. 7(c)]. The only difference is that the xxy spectrum appears to be a down-scaled yxy spectrum. For example, they both increase rapidly above the absorption edge of 1.33 eV and then peak at ~ 1.9 eV. As photon energy further increases, the two spectra decrease sharply and become nearly zero at ~ 2.0 eV. After that, they increase again with photon energy. The circular shift currents [Fig. 7(c)] appear to be two-orders of magnitude smaller than the linear injection currents [Fig. 7(b)]. Nonetheless, the size of the circular shift currents is comparable to that of the linear shift currents in archetypal semiconductors with a similar band gap such as CdSe [31].

Let us now compare the photocurrents of BL CrI₃ with the well-known BPVE materials to examine the possibility of BL CrI₃ for photovoltaic solar cell applications. The predicted shift photocurrent conductivity of the well-known ferroelectric materials of PbTiO₃ and BiTiO₃ have a maximum value of $5 \mu\text{A}/\text{V}^2$ within the visible region below 6 eV. This is much smaller than that of BL CrI₃. Nevertheless, the predicted shift current conductivity of the chiral materials has the highest value of $\sim 80 \mu\text{A}/\text{V}^2$ in the visible light [52]. The experimental reported maximum value of the shift photocurrent conductivity within the visible range is $6 \mu\text{A}/\text{V}^2$ for semiconductor SbSI [53]. All these comparisons indicate that the magnetism-induced photocurrent in BL CrI₃ is very large. Furthermore, compared with ferroelectric oxides such as PbTiO₃ and BiTiO₃, BL CrI₃ has a much smaller band gap and thus has a high solar energy absorption efficiency. Therefore, BL CrI₃ will be a promising material for high efficient photovoltaic solar cell application.

4. Conclusion

In conclusion, we have calculated AF-induced NLO responses of the AB'-stacked centrosymmetric BL

CrI₃ based on the GGA+U method. Strikingly, we find that the magnetic SHG, LEO and photocurrent in the AF BL CrI₃ are very large, being comparable or even larger than the well-known nonmagnetic noncentrosymmetric semiconductors with the same properties. For example, the calculated SHG coefficients are in the same order of magnitude as that of MoS₂ ML, the most promising 2D material for NLO devices. The calculated LEO coefficients are almost three times larger than that of MoS₂ ML. The calculated NLO photocurrent in BL CrI₃ is among the largest values predicted so far for the bulk photovoltaic materials. On the other hand, unlike nonmagnetic semiconductors, the NLO responses in the AF BL CrI₃ are nonreciprocal and also switchable by rotating magnetization direction. Therefore, our interesting findings show that the AF BL CrI₃ will find valuable applications in magnetic NLO and LEO devices such as frequency conversion, electro-optical switches, and light signal modulators as well as high energy conversion efficiency photovoltaic solar cells.

Note added – After submitting our manuscript, we became aware of the work by Song *et al.*, [54] who independently performed the *ab initio* calculation on the SHG in the AF BL CrI₃ based on the velocity gauge formalism instead of length gauge formalism adopted here.

Acknowledgement: G.-Y. Guo thanks Jun-yeong Ahn and Naoto Nagaosa for helpful discussions on NLO photocurrent and bulk photovoltaic effect. The authors acknowledges the support by the Ministry of Science and Technology, National Center for Theoretical Sciences and National Center for High-performance Computing in Taiwan. G.-Y. Guo also thanks the support from the Far Eastern Y. Z. Hsu Science and Technology Memorial Foundation in Taiwan.

References:

- [1] Gong C, Li L, Li Z, Ji H, Stern A, Xia Y, Cao T, Bao W, Wang C, Wang Y, Qiu Z Q, Cava R J, Louie S J, Xia J and Zhang X 2017 *Nature* **546** 265.
- [2] Huang B, Clark G, Navarro-Moratalla E, Klein D R, Cheng R, Seyler K L, Zhong D, Schmidgall D, McGuire M A, Cobden D H, Yao W, Xiao D, Jarillo-Herrero P and Xu X 2017 *Nature* **546** 270.
- [3] Seyler K L, Zhong D, Klein D R, Gao S, Zhang S, Huang B, Navarro-Moratalla E, Yang L, Cobden D H, McGuire M A, Yao W, Xiao D, Jarillo-Herrero P and Xu X 2018 *Nat. Phys.* **14** 277.
- [4] Huang B, Clark G, Klein D R, MacNeill D, Navarro-Moratalla E, Seyler K L, Wilson N, McGuire M A, Cobden D H, Xiao D, Yao W, Jarillo-Herrero P and Xu X 2018 *Nat. Nanotechnol.* **13** 544.
- [5] Jiang S, Shan J and Mak K F 2018 *Nat. Mater.* **17** 406.
- [6] Jiang S, Li L, Wang Z, Mak K F and Shan J 2018 *Nat. Nanotechnol.* **13** 549.
- [7] Kim H H, Yang B, Patel T, Sfigakis F, Li C, Tian S, Lei H and Tsen A W 2018 *Nano Lett.* **18** 4885.
- [8] Klein D R, MacNeill D, Lado J L, Soriano D, Navarro-Moratalla E, Watanabe K, Taniguchi T, Manni S, Canfield

- P, Fernández-Rossier J and Jarillo-Herrero P 2018 *Science* **360** 1218.
- [9] Song T, Cai X, Tu M W-Y, Zhang X, Huang B, Wilson N P, Seyler K L, Zhu L, Taniguchi T, Watanabe K, McGuire M A, Cobden D H, Xiao D, Yao W and Xu X 2018 *Science* **360** 1214.
- [10] Sivadas N, Okamoto S, Xu X, Fennie C J and Xiao D 2018 *Nano Lett.* **18** 7658.
- [11] Jiang P, Wang C, Chen D, Zhong Z, Yuan Z, Lu Z-Y and Ji W 2019 *Phys. Rev. B* **99** 144401.
- [12] Soriano D, Cardoso C and Fernández-Rossier 2019 *J. Solid State Commun.* **299** 113662.
- [13] Jang S W, Jeong M Y, Yoon H, Ryee S and Han M J 2019 *Phys. Rev. Materials* **3** 031001(R).
- [14] Sun Z, Yi Y, Song T, Clark G, Huang B, Shan Y, Wu S, Huang D, Gao C, Chen Z, McGuire M A, Cao T, Xiao D, Liu W-T, Yao W, Xu X and Wu S 2019 *Nature* **572** 497.
- [15] Shen Y R 2003 *The Principle of Nonlinear Optics* (John Wiley and Sons Inc., New Jersey, 2003).
- [16] Boyd R W 2003 *Nonlinear Optics* (Elsevier Science, Amsterdam, 2003).
- [17] Zhang Y, Holder T, Ishizuka H, de Juan F, Nagaosa N, Felser C and Yan B 2019 *Nat. Commun.* **10** 3783.
- [18] McGuire M A, Dixit H, Cooper V R and Sales B C 2015 *Chem. Mater.* **27** 612.
- [19] Gudelli V K and Guo G-Y 2019 *New J. Phys.* **21** 053012.
- [20] Perdew J P, Burke K and Ernzerhof M 1996 *Phys. Rev. Lett.* **77** 3865.
- [21] Dudarev S L, Botton G A, Savrasov S Y, Humphreys C J and Sutton A P 1998 *Phys. Rev. B* **57** 1505.
- [22] Fang Y, Wu S, Zhu Z-Z and Guo G-Y 2019 *Phys. Rev. B* **98** 125416.
- [23] Bloechl P E *Phys. Rev. B* **50** 17953.
- [24] Kresse G and Joubert D 1999 *Phys. Rev. B* **59** 1758.
- [25] Kresse G and Furthmüller J 1996 *Phys. Rev. B* **54** 11169.
- [26] Kresse G and Furthmüller J 1996 *Comput. Mat. Sci* **6** 15.
- [27] Aversa C and Sipe J E 1995 *Phys. Rev. B* **52** 14636.
- [28] Wu Q and Zhang X-C 1996 *Appl. Phys. Lett.* **68** 14636.
- [29] Veithen M, Gonze X and Ghosez P 2005 *Phys. Rev. B* **71** 125107.
- [30] Sipe J E and Shkrebtii A. I *Phys. Rev. B* **61** 5337.
- [31] Nastos F and Sipe J E 2010 *Phys. Rev. B* **82** 235204.
- [32] Ahn J, Guo G-Y and Nagaosa N 2020, *Phys. Rev. X* (2020) (in press) (arXiv:2006.06709v2).
- [33] Wang C-Y and Guo G-Y 2015 *J. Phys. Chem. C* **119** 13268.
- [34] Guo G Y and Lin J C 2005 *Phys. Rev. B* **72** 075416.
- [35] Guo G Y and Lin J C 2008 *Phys. Rev. B* **77** 049901(E).
- [36] Wu I J and Guo G Y *Phys. Rev. B* **78** 035447.
- [37] Wang X, Yates J R, Souza I, and Vanderbilt D, *Phys. Rev. B* **74**, 195118 (2006).
- [38] Marzari N, Mostofi A A, Yates J R, Souza I, and Vanderbilt D, *Rev. Mod. Phys.* **84**, 1419 (2012).
- [39] Ibanez-Azpiroz J, Tsirkin S S and Souza I *Phys. Rev. B* **97**, 245143 (2018).
- [40] J. F. Dillon Jr. and C. E. Olson, *J. Appl. Phys.* **36**, 1259 (1965).
- [41] J. Heyd, *J. Chem. Phys.* **118**, 8207 (2003).
- [42] J. Heyd, G. E. Scuseria, and M. Ernzerhof, *J. Chem. Phys.* **124**, 219906 (2006).
- [43] Gallego S V, Etxebarria J, Elcoro L, Tasci E S and Perez-Mato J M 2019 *Acta Cryst. A* **75**, 438.
- [44] Pan R-P, Wei H D and Shen Y R 1989 *Phys. Rev. B* **39** 1229.
- [45] Reif J, Zink J C, Schneider C-M and Kirschner J 1991 *Phys. Rev. Lett.* **67** 2878.
- [46] Li Y, Rao Y, Mak K F, You Y, Wang S, Dean C R and Heinz T F 2013 *Nano Lett.* **13** 3329.
- [47] Kumar N, Najmaei S, Cui Q, Ceballos F, Ajayan P M, Lou J and Kumar H Z 2013 *Phys. Rev. B* **87** 161403(R).
- [48] Malard L M, Alencar T V, Barboza A P M, Mak K F and de Paula A M 2013 *Phys. Rev. B* **87** 201401(R).
- [49] Guyot-Sionnest P, Chen W and Shen Y R 1986 *Phys. Rev. B* **33** 8254.
- [50] Trassin M, Luca D, G, Manz S and Fiebig M 2015 *Adv. Mater.* **27** 4871.
- [51] Matsubara M, Manz S, Mochizuki M, Kubacka T, Iyama A, Aliouane N, Kimura T, Johnson S L, Meier D and Fiebig M 2015 *Science* **348** 1112.
- [52] Zhang Y, de Juan Y, Grushin A G, Felser C and Sun Y 2019 *Phys. Rev. B* **100** 245206.
- [53] Sotome M, Nakamura M, Fujioka J, Ogino M, Kaneko Y, Morimoto T, Zhang Y, Kawasaki M, Nagaosa N, Tokura Y and Ogawa N 2019 *Proc. Natl. Acad. Sci.* **116** 1929.
- [54] Song W, Fei R, Zhu L and Yang L, *Phys. Rev. B* **102**, 045411 (2020).